

Spin and orbital Hall effect in non-magnetic transition metals: extrinsic vs intrinsic contributions.

Sergiy Mankovsky¹ and Hubert Ebert¹

¹*Department Chemie, Physikalische Chemie, Universität München, Butenandtstr. 5-13, 81377 München, Germany*

Kubo's linear response formalism has been used to calculate the orbital Hall conductivity (OHC) for non-magnetic undoped and doped transition metal systems, focusing on the impact of different types of disorder and the role of vertex corrections for the OHC. The doping- and temperature-dependence of the OH conductivity have been investigated and compared with corresponding results for the spin Hall conductivity (SHC). A strong difference has been found between the results for undoped and doped metallic systems. For elemental systems at finite temperature a dominating role of the intrinsic contribution to the temperature-dependent OH and SH conductivities is found. Moreover, the different temperature dependent behavior of the intrinsic SOC-independent OHC and SOC-driven SCH indicates a non-trivial relationship between these quantities. It is shown, that in contrast to the intrinsic part of the OH and SH conductivities, the extrinsic contributions in doped systems are determined by spin-orbit coupling for both of them. It is dominating at low temperature, strongly decreasing at higher temperatures due to the increasing impact of the electron-phonon scattering.

I. INTRODUCTION

The occurrence of a spin current in solids in the direction perpendicular to an applied electric field, called spin Hall effect (SHE), is a well established phenomenon studied both experimentally and theoretically. This effect is broadly discussed in the literature concerning its origin, showing in particular that its intrinsic contribution is determined by topological features of the electronic band structure, while the extrinsic part is seen as a consequence of asymmetric electron scattering in the presence of different types of disorder in the material (see, e.g., Ref. [1] and references therein). Another type of Hall effect, called orbital Hall effect (OHE), predicted for doped semiconductors² and for transition metals³, implies for a finite sample an angular momentum accumulation due to the angular momentum flow in the direction perpendicular to applied electric field. The origin of the OHE is still under discussion. In contrast to the spin Hall conductivity (SHC), representing the SHE, the intrinsic orbital Hall conductivity (OHC) connected to the OHE is almost independent of the spin-orbit coupling (SOC). Moreover, the sign of the OHC can differ from that of the SHC^{3,4}. Tanaka et al.⁵ and H. Kontani et al.³ concluded that the OHC has to be always positive for $4d$ and $5d$ transition metals. On the other hand, recent findings by Go et al.⁴ demonstrate, that the intrinsic OHC can have a negative sign for some late $3d$, $4d$ and $5d$ elements. Discussing the origin of the SHE and OHE, Kontani et al.³ have shown that the SHE in transition metals may be seen as a SOC-driven spin flow accompanying the transverse flow of orbital angular momentum in the presence of an applied electric field. As a consequence, the SHC may be approximated by the product of the OHC and the spin polarization at the Fermi energy, arising due to the SOC³. This explains in particular, the reason, why the intrinsic OHC exceeds the SHC, as well as why they have different sign for some materials.

Coming to the origin of the intrinsic OHE, the transverse orbital angular momentum flow induced by an applied electric field may be seen as a consequence of the orbital texture in momentum space⁶, even if the orbital angular momentum at each atomic site \vec{l}_i is completely quenched in equilibrium. Thus, Go et al.⁷ suggested a mechanism giving rise for the OHC, following an idea of the Sinova et al.⁸ to explain the origin of the intrinsic SHE. The latter mechanism implies a spin current arising due to the spin texture in momentum space, which is induced by spin orbit coupling (SOC) and therefore is seen as a relativistic effect in contrast to the OHE. According to the suggestion by Go et al.⁷, a finite k -dependent orbital angular momentum in reciprocal space can be dynamically induced without SOC but due to a field-induced excitation of the electronic structure, leading at the end to a non-vanishing orbital current. A giant orbital Hall effect for a broad class of centrosymmetric materials was reported by various authors on the basis of theoretical investigations^{4,5,9-11}. Furthermore, several theoretical predictions have been confirmed also experimentally. In particular, an electric field induced orbital angular momentum accumulation has been observed recently also experimentally in non-magnetic¹² as well as in magnetic materials¹³.

In the case of doped materials and random alloys, the conductivity tensor will be modified due to the impact of disorder. For instance, a modification of the SHE due to disorder may occur, on the one hand side, as a result of corresponding modification of the electronic structure having an impact on the intrinsic part of the SHE. On the other hand, the SOC-driven asymmetric scattering of the charge carriers with opposite spin (skew scattering and side-jump scattering) leads to the extrinsic contribution which may strongly modify the SH conductivity (see, e.g.^{1,14,15}).

In the case of the OHE, only few results have been reported in the literature so far, which concern the impact

of disorder on the OHC. In the case of p -doped silicon studied using the Luttinger model, it was shown that the vertex corrections due to impurity scattering vanish identically, and the OHE is represented essentially by the intrinsic contribution². On the other hand, Tanaka et al.⁵ reported about a finite correction to the OHC calculated for transition metals, which is introduced by disorder.

Tang and Bauer¹⁶ have also investigated the role of disorder for the OHE solving the quantum Boltzmann equation. They have shown that the corrections to the OHC due to disorder are very sensitive to the scattering potential and pointed out that the predictions by Bernevig et al.² are valid only in the limit of a short-range scattering potential. Using a finite-range scattering potential, Tang and Bauer calculated the correction to the OHE due to diffuse scattering which was taken into account via a scattering-in contribution to the collision term in the Boltzmann equation. These calculations already demonstrated the important role of disorder for the OHC. Based also on the findings of previous works (see, e.g. Refs. [5 and 15]), which concern the role of the scattering potential for the SHE and OHE, one can conclude that first principles calculations of the OHC are of great importance to get reliable results on the extrinsic contribution to this quantity. A strong impact of disorder on the OHC has been reported recently by Liu and Culcer¹⁷ who investigated the OHE in graphene and transition metal dichalcogenides. They found that the extrinsic OHC in doped systems provides the dominant contribution to the OHE in the case when the Fermi level crosses the conduction or valence bands. The authors attribute this extrinsic effect to the skew and side jump scattering, making use of the analogy with the SHE in the investigated materials. One has to note in addition, that there is no explicit discussion in the literature so far concerning the scattering mechanisms responsible for the asymmetric scattering of the electrons with different orbital angular momentum. Expecting that the scattering asymmetry of the orbital and spin angular momentum are closely connected to each other due to SOC, we will discuss and compare the various scattering mechanisms both for the OHE and SHE.

Below, we will present the results of first principles calculations for the OHC and SHC. We will compare the properties of the OHC and SHC for pure materials, calculated for finite temperature, discussing both contributions, extrinsic and intrinsic, and demonstrate how these contributions depend on temperature. Next, we will deal with doped transition metal systems, and will discuss the concentration and temperature dependence properties of the extrinsic and intrinsic OHC in comparison with the SHC. Moreover, we will demonstrate the crucial role of spin-orbit interaction on the extrinsic contribution both for the OHE and the SHE.

II. THEORETICAL DETAILS

Here we will describe some technical details relevant for the discussions below on the results of our calculations. As the calculations of the OH and SH conductivities are closely connected to each other, all discussions of their properties will be done in parallel. This takes into account, that the properties of the SHE were already previously investigated and discussed extensively in the literature^{1,8,18,19}.

The calculations of the OHC, similar to the SHC^{20–23}, are based on Kubo's linear response formalism using the so-called Bastin formula²⁴ (for more details see the Appendix). The underlying electronic structure is calculated making use of the fully relativistic KKR Green's function method^{25,26}. The OH and SH conductivity tensors are calculated accounting for the vertex corrections^{22,23,27} to describe properly the corresponding transport properties in the presence of various types of disorder. Formally a corresponding conductivity tensor element may be written as follows²⁰ (omitting the angular momentum indices):

$$\sigma_{\mu\nu}^{\text{VC}} \propto \text{Tr} J_{\mu}(z_2, z_1) [(1 - \chi w)^{-1} \chi] j_{\nu}(z_1, z_2). \quad (1)$$

The current density operator \vec{j} representing the perturbation j_{ν} with corresponding matrix elements is given in relativistic form by $\vec{j} = e c \underline{\alpha}$ with the velocity operator $\vec{v} = c \underline{\alpha}$ and $\underline{\alpha}_{\mu}$ the standard Dirac matrices. For calculations of the SHC, the response function is given by the spin current density operator $\hat{J}_{\mu}^{\text{s},\beta}$ ^{21,23}. The OHC is calculated using for the response orbital current density the operator given by the expression $\hat{J}_{\mu}^{\text{o},\beta} = \frac{1}{2} c (\hat{l}^{\beta} \underline{\alpha}_{\mu} + \underline{\alpha}_{\mu} \hat{l}^{\beta})$, where \hat{l} is the orbital angular momentum operator. Below we will use the shorthand notation σ_{SH} and σ_{OH} for the tensor elements $\sigma_{xz}^{(\text{S}),y}$ and $\sigma_{xz}^{(\text{O}),y}$ of the spin polarization and orbital polarization conductivity tensors, respectively.

As it was discussed in the literature (see, e.g., Refs. [1, 14, and 23]), the extrinsic SHE is associated with the vertex corrections to the expression for the conductivity tensor, which account for the SOC-driven side-jump and skew scattering in the electron transport. Expanding the term $(1 - \chi w)^{-1}$ accounting for vertex corrections in a Taylor series, leads to the expression

$$\sigma_{\mu\nu}^{\text{VC}} \propto \sigma_{\mu\nu}^{\text{NVC}} + J_{\mu}(z_2, z_1) [\chi w \chi + \chi w \chi w \chi + \dots] j_{\nu}(z_1, z_2). \quad (2)$$

from which one can see that the difference $\sigma_{\mu\nu}^{\text{VC}} - \sigma_{\mu\nu}^{\text{NVC}}$ characterizes the extrinsic contribution to the SHC. Accordingly, the intrinsic part of the SHE may be obtained by performing the calculations without vertex corrections. The same refers also to the OHC. It is important to remind also, that the vertex corrections, giving the extrinsic contribution to the SHC, are associated with the Fermi surface electrons²⁸. In the superclean regime (i.e. with the impurity concentration $x \rightarrow 0$) the scattering is dominated by the skew-scattering mechanism²⁹ and the

SHC is linearly connected with the electrical longitudinal conductivity $\sigma_{\mu\mu}$ according to $\sigma_{\mu\nu}^{(S)\text{skew}} = S \sigma_{\mu\mu}$, where S is the so-called skewness factor. This implies, that $\sigma_{\mu\nu}^{\text{skew}}$ diverges together with $\sigma_{\mu\mu}$ as $1/x$ in the pure limit. In contrast to the skew scattering, the side jump and intrinsic contributions in the low-concentration regime are often comparable in magnitude and weakly depend on impurity content^{23,30,31}. As a result, the SHC can be represented by the expression

$$\sigma_{\mu\nu}^{(S)} = \sigma_{\mu\nu}^{(S)\text{intrinsic}} + \sigma_{\mu\nu}^{(S)\text{sj}} + S \sigma_{\mu\mu}. \quad (3)$$

Assuming that the same scattering mechanisms are responsible for the extrinsic OHC as well, we will discuss below the skew scattering and side jump contributions also for the OHC.

In order to investigate the impact of the SOC on the SHC and OHC, corresponding calculations have been performed applying a scaling of the speed of light c allowing a continuous transition from the relativistic description of transport properties (i.e., without scaling $c = c_0$) to the non-relativistic limit corresponding to $c = \infty$. As the leading relativistic corrections to the Schrödinger Hamiltonian vary as $1/c^2$, we will use the scaling parameter $\xi = (\frac{c_0}{c})^{232}$. It will be referred to in the discussions below as the SOC scaling factor, assuming that among all the relativistic effects, SOC has the dominating impact on the SHC and OHC.

The calculations have been performed using the spin-polarized relativistic KKR Green function method^{26,33} in combination with the atomic sphere approximation (ASA). The exchange-correlation potential was calculated within the local spin density approximation (LSDA) to spin density functional theory (SDFT), using a parametrization as given by Vosko et al.³⁴. The angular momentum expansion of the Green function was cut-off at $l_{\text{max}} = 3$. A k -mesh including up to 10^8 grid points in the full Brillouin zone (BZ) was used for the integration over the BZ when calculating the conductivity tensors.

The temperature dependent properties of the OHC and SHC have been investigated by accounting for the impact of thermally induced lattice vibrations, assuming that the effects of the temperature dependent Fermi-Dirac distribution function can be neglected in the temperature regime under consideration. These calculations have been performed making use of the alloy analogy model³⁵ based on the adiabatic approximation, that implies that a discrete set of N_v displacement vectors $\Delta\vec{R}_v^q(T)$ with probability x_v^q ($v = 1, \dots, N_v$) is constructed for each basis atom q within the crystallographic unit cell. The vectors $\Delta\vec{R}_v^q(T)$ are connected with the temperature dependent root mean square displacement $(\langle u^2 \rangle_T)^{1/2}$ according to the relation:

$$\sum_{v=1}^{N_v} x_v^q |\Delta\vec{R}_v^q(T)|^2 = \langle u_q^2 \rangle_T. \quad (4)$$

For the applications presented below, the temperature dependent root mean square displacement is estimated

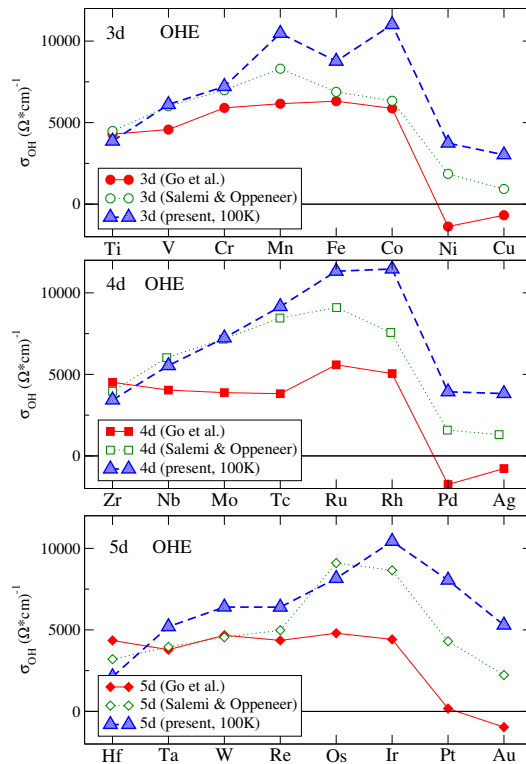


FIG. 1. Orbital Hall conductivity σ_{OH} for the elemental paramagnetic 3d, 4d and 5d materials, calculated for $T = 100\text{K}$ in comparison with the results by Go et al.⁴ and Salemi and Oppeneer³⁶ for $T = 0\text{K}$.

using Debye's theory, providing a simple connection between $\langle u_q^2 \rangle_T$ and the lattice temperature.

III. RESULTS

In this section we will consider two types of non-magnetic materials, undoped and doped. In the latter case we will show the impact of chemical disorder on the OHC discussing it in parallel with the SHE. Furthermore, for both types of materials we will discuss the temperature dependence of the OHC and SHC.

A. Elemental transition metal materials at finite temperature.

First, we compare our results for elemental 3d, 4d and 5d transition metals with some first-principles results available in the literature. This comparison can be seen in Figs. 1 and 2 for the OHC and SHC, respectively. For numerical reason the present calculations were performed for the lattice temperature $T = 100\text{K}$. The temperature was taken low enough to avoid a noteworthy temperature dependent extrinsic contribution to the Hall effects caused by the electron scattering by lattice vibrations.

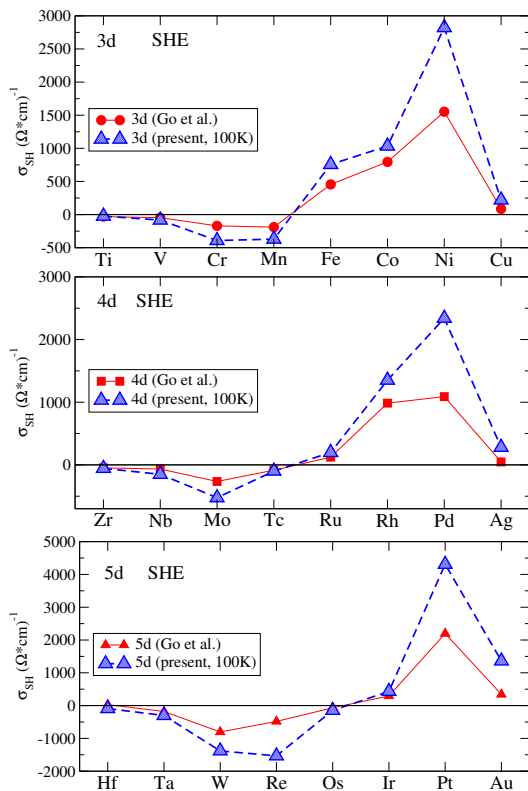


FIG. 2. Spin Hall conductivity σ_{SH} for the elemental paramagnetic 3d, 4d and 5d materials, calculated for $T = 100\text{K}$ in comparison with the results by Go et al.⁴ for $T = 0\text{K}$.

This ensures that the obtained results can be directly compared with the results by other groups giving the intrinsic OHC and SHC^{4,10} for $T = 0\text{K}$. One can see a reasonably good agreement between the various results, with the difference partly attributable to the finite temperature assumed for the calculations in the present case.

The effect of a finite temperature on the OHC and SHC of pure transition metals has been investigated in some details for temperatures up to 600 K. Fig. 3 shows the total (full circles) and extrinsic (open circles) OHC for some selected transition metals, plotted as a function of temperature. Note that the latter quantity is determined by the Fermi surface contribution $\sigma_{\text{OH}}^{\text{extr}} = \sigma_{1,\text{OH}}^{\text{VC}}(E_F) - \sigma_{1,\text{OH}}^{\text{NVC}}(E_F)$, while vertex corrections to the Fermi sea contribution to the OHC are negligibly small, in line with the findings in Ref. [37] (see also the comments in the Appendix). Similar plots are done also for the total (full squares) and extrinsic (open squares) SHC.

For all systems the intrinsic OHC and SHC are dominating in the low-temperature limit. The extrinsic contributions are almost unchanged for the temperature window shown in Fig. 3. This should imply a negligibly small impact of the electron-phonon skew scattering events on the extrinsic OHC and SHC. Otherwise, skew scattering would lead to their diverging behavior in the limit

of $T = 0\text{K}$ similar to the electrical conductivity. Accordingly, one can conclude that the extrinsic OHC and SHC can be attributed primarily to the impact of the side jump scattering events. Interestingly, this contribution practically does not depend on temperature, similar to weak concentration dependence of the side jump SHC in doped systems. However, one has to keep in mind that such an analogy is not one-to-one. In Fig. 4 the extrinsic OHC, $\sigma_{\text{OH}}^{\text{extr}}$, and SHC, $\sigma_{\text{SH}}^{\text{extr}}$, are plotted for Pd and Pt versus the electrical conductivity $\sigma_{\mu\mu}$. Due to the relationship

$$\sigma_{\text{OH/SH}}^{\text{extr}} = \sigma_{\text{OH/SH}}^{\text{skew}} + \sigma_{\text{OH/SH}}^{\text{sj}} = S_{\text{OH/SH}}\sigma_{\mu\mu} + \sigma_{\text{OH/SH}}^{\text{sj}}, \quad (5)$$

an extrapolation to $\sigma_{\mu\mu} = 0$ gives access to the electron-phonon side-jump contributions to the OHC and SHC in the low-temperature limit. This is a dominating contribution to the finite-temperature extrinsic OHC and SHC in Pt and only to the SHC in Pd while both the side-jump and skew scattering parts are extremely small. Note that the side-jump contributions strongly depend on the material, as it follows from the results shown in Fig. 3. This brings us to a conclusion concerning the properties of the OHC and SHC originating from thermal lattice vibrations: a contribution due to skew scattering to the extrinsic OHC and SHC in pure metals is rather small, and the extrinsic OHC and SHC are dominated by the side-jump scattering mechanism. These results are in line with theoretical predictions for the anomalous Hall effect, reported by Crépieux and Bruno¹⁴. They attributed this effect to the fluctuating sign of the scattering potential associated with thermal phonons, which leads to a canceling effect of skew scattering changing sign together with the scattering potential³⁸.

Note that only few experimental results have been reported for the temperature dependence of the OHC for pure metals. While a dominating intrinsic contribution to the SHC has been found for Pt³⁹, in line with the results of our calculations, the temperature dependent variation of the OHC in Au³⁹ as well as in Pt⁴⁰ was associated with the electron-phonon skew scattering. It is worth noting, however, that the samples used in these experiments are characterized by a finite residual resistivity. This is a crucial point, that will be discussed below, since the impact of electron-phonon scattering on the temperature dependence of the OHC and SHC strongly changes in the case of doped systems. Of course, one cannot exclude some discrepancies between theory and experiment, originating from the approximations used in the calculations.

Thus, the obtained results show essential temperature-dependent changes of the intrinsic OHC in pure transition metals, associated with corresponding changes of the Fermi sea contribution, while the Fermi surface part exhibits only a weak variation with temperature. This can be attributed to the changes of the electronic structure arising due to thermal lattice vibrations leading first of all to a smearing of the energy bands implying a decreasing

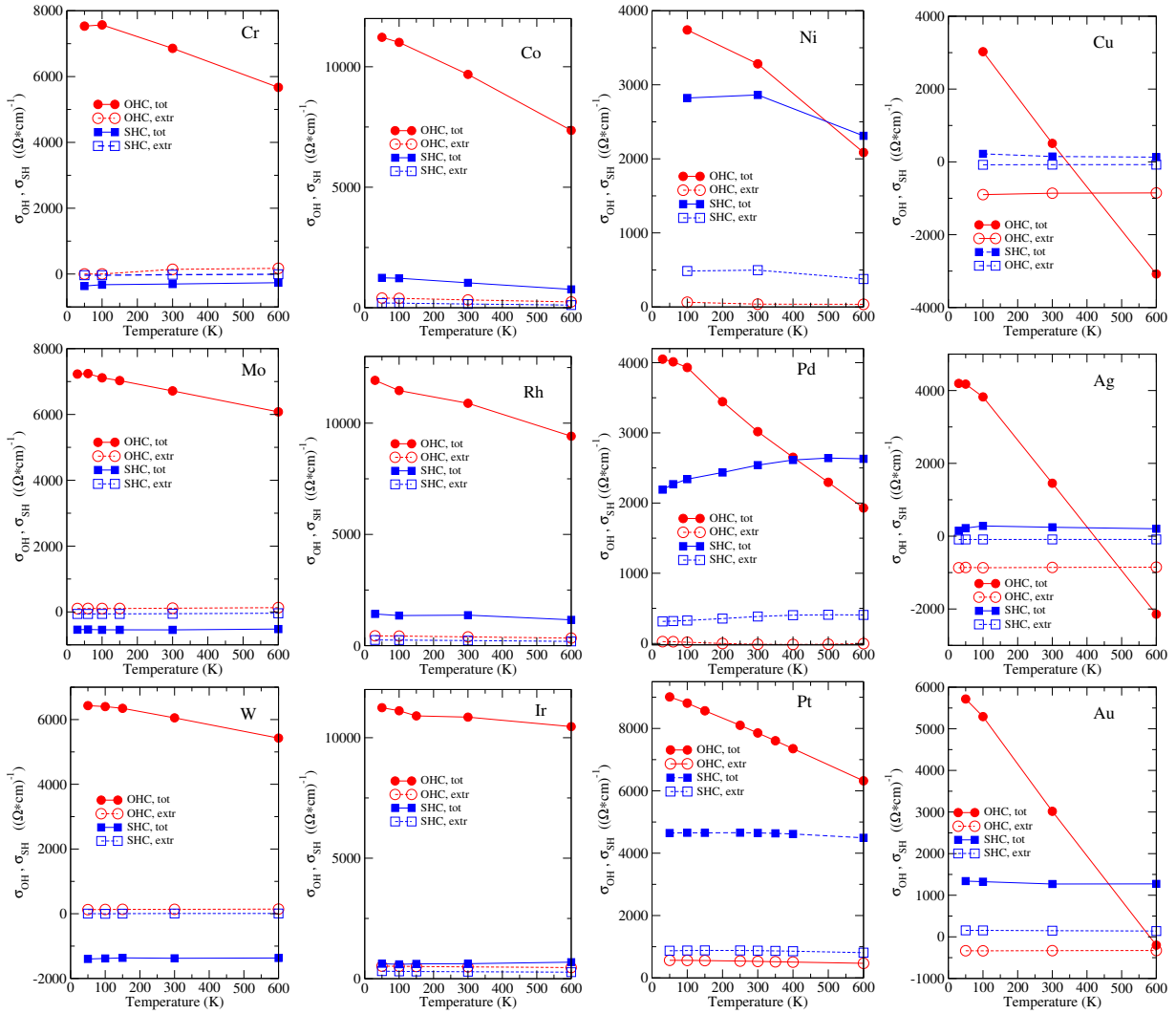


FIG. 3. OH and SH conductivities (full red circles and full blue squares, respectively) for selected elemental $3d$, $4d$ and $5d$ non-magnetic metals, calculated accounting for thermal lattice vibrations and plotted as a function of temperature. Empty symbols represent the extrinsic contributions to the OHC and SHC.

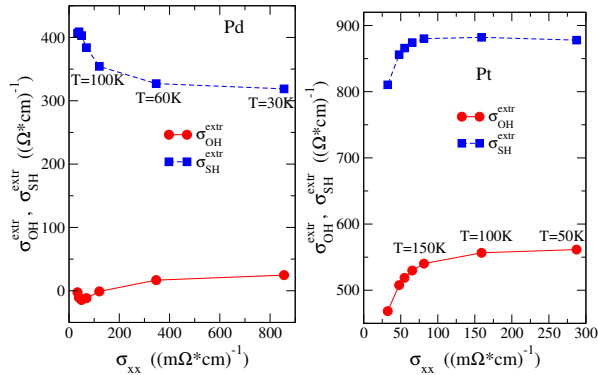


FIG. 4. Temperature dependent extrinsic OH and SH conductivities $\sigma_{\text{OH}}^{\text{extr}}(T)$ and $\sigma_{\text{SH}}^{\text{extr}}(T)$, for Pd and Pt, represented as a function of electrical conductivity.

lifetime of the electronic states. In contrast to the OHC, a weak temperature-induced change can be seen for both the intrinsic and extrinsic contributions to the SHC. To gain insight into to origin for this different behavior we have performed calculations for the OHC and SHC as a function of the occupation of the electron states, using Ag as a representative system as it has a rather strong variations of the OHC with temperature. In the calculations, the occupation is controlled by the upper energy limit E_{occ} which is equal to E_F under normal condition. The calculations have been done for two lattice temperatures, $T = 100$ and $T = 600$ K. Fig. 5(a) shows the results for total OHC and SHC, which, however, are mainly determined by the intrinsic contributions, as it is shown in Fig. 3. One can see in Fig. 5(a) (bottom) a minor difference between the results for the SHC obtained for two different temperatures, that, however, is not the case for the OHC

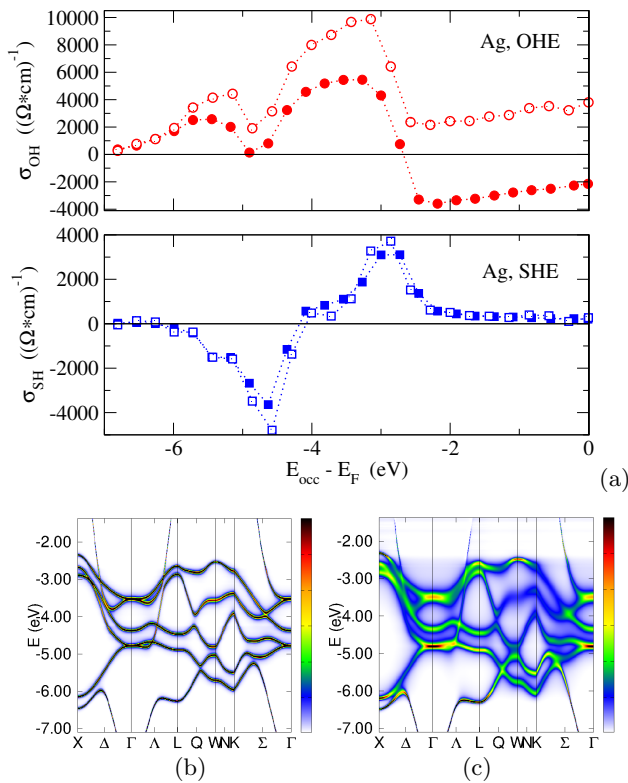


FIG. 5. (a) The OHC, $\sigma_{OH}(E_{occ})$ (top) and SHC, $\sigma_{SH}(E_{occ})$ (bottom) calculated for Ag at $T = 100$ (open symbols) and $T = 600$ K (full symbols), represented as a function of occupation of electron states E_{occ} . (b) and (c) The BSF for Ag at $T = 100$ and $T = 600$ K, respectively.

(Fig. 5(a), top). The difference between the results for the OHC at $T = 100$ and $T = 600$ K increases together with increasing occupation, i.e. E_{occ} , of the d -states, and almost does not change when E_{occ} goes beyond the top of the d -band. This occupation dependence, in particular, may be responsible for a weaker temperature dependence of the OHC for the early transition metals. The strong temperature-induced modification of the OHC can be attributed to the impact of thermal lattice vibrations on the electronic structure leading to a strong smearing of the energy bands, increasing with temperature. This can be seen in the bottom panel of Fig. 5 that gives the Bloch spectral function $A(\vec{k}, E, T)$ for Ag, calculated for $T = 100$ (b) and $T = 600$ K (c). Furthermore, it is crucial that the temperature-induced lattice distortion breaks local symmetry at each lattice site. As soon as the origin of the OHE is associated with the \vec{k} -dependent orbital texture controlled by symmetry^{3,4,6,11,16}, the OHC variation at finite temperature may stem from broken local symmetry at every atomic position, leading to a modification of the orbital texture, increasing with temperature (see also discussions in Ref. [16]). Interestingly, only minor changes occur for the SHC, in conflict with the idea that the SOC-driven spin Hall current density originates from the orbital Hall current density³. This indicates in

particular that the relationship between these quantities is not straightforward.

B. Doped materials

1. Doping effect in OHC and SHC.

Next, we discuss the properties of the OHC in the presence of disorder in doped materials, and compare the results with corresponding properties of the SHC.

We consider first, two arbitrary chosen doped systems: (i) one with the host and impurity atoms corresponding to different transition metal periods but having the same number of valence electrons, $\text{Ag}_{1-x}\text{Au}_x$, and (ii) another one with the host and impurity atoms which belong to the same periods but with different number of valence electron, $\text{Rh}_{1-x}\text{Ag}_x$. The corresponding results for the OHC and SHC are plotted in Fig. 6(a) and (b) (full circles for the OHC and full squares for the SHC), respectively, as a function of concentration. One can see a divergent behavior for the OHC and SHC for $\text{Ag}_{1-x}\text{Au}_x$ towards the pure limit, which however is hardly seen in the case of $\text{Rh}_{1-x}\text{Ag}_x$. The reason for this difference is discussed next.

As is shown in Fig. 6 (a), a strong increase of the OHC and SHC towards the pure limit ($x \rightarrow 0$) in $\text{Ag}_{1-x}\text{Au}_x$ is mainly determined by the extrinsic contribution arising due to skew-scattering. This conclusion follows from the relationship $\sigma_{OH/SH}^{\text{skew}} = S_{OH/SH}\sigma_{\mu\mu}$ between the skew-scattering contributions to the extrinsic OHC and SHC and the electrical conductivity, which is demonstrated in Fig. 6(c). As one can see, the total and extrinsic OHC and SHC are lying almost on top of each other, and the extrapolation to the limit $\sigma_{\mu\mu} = 0$ (see Section II) leads to small values for the intrinsic as well as side-jump extrinsic contributions to the OHC and SHC. This finding gives an evidence that the same skew scattering mechanism should be responsible for both the OHC and SHC in $\text{Ag}_{1-x}\text{Au}_x$, although the skewing factors are different for the OHC and SHC. This conclusion is also in line with the results for the SOC dependence of the extrinsic OHC and SHC shown in Fig. 7 for $\text{Ag}_{1-x}\text{Au}_x$, with the SOC strength controlled via the scaling factor ξ . For the sake of convenience, the same data are plotted using a linear (a) and a logarithmic (b) scale for the ordinate axis. In Fig. 7(a) one can see a quick decrease in magnitude for the total OHC and SHC (which are negative) followed by a variation of the extrinsic contributions corresponding to the SOC reduction with the scaling factor decreasing from $\xi = 1$ to the value $\xi \approx 0.7$ for which both the OHC and SHC change sign. A further decrease of the scaling factor $\xi \rightarrow 0$ leads to the decrease of a positive extrinsic and total OHC and SHC (see Fig. 7(b)). In the limit of $\xi = 0$ (i.e. no SOC), the extrinsic OHC vanishes and the total OHC coincides with its intrinsic contribution. The total SHC decreases due to a decrease of both contributions, extrinsic and intrinsic, and vanishes in the limit of

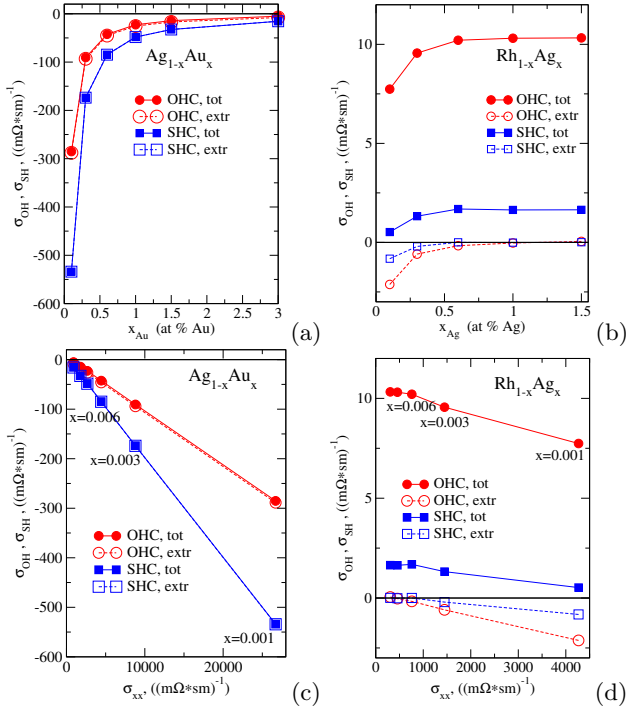


FIG. 6. OH (circles) and SH (squares) conductivities for $\text{Ag}_{1-x}\text{Au}_x$ (a) and $\text{Rh}_{1-x}\text{Ag}_x$ (b) around the Ag-rich and Rh-rich limits, respectively, as a function of the impurity concentration. OH (circles) and SH (squares) conductivities plotted as a function of the electrical conductivity for $\text{Ag}_{1-x}\text{Au}_x$ (c) and $\text{Rh}_{1-x}\text{Ag}_x$ (d), respectively. Full symbols in all figures correspond to the total OHC and SHC, while open symbols represent the extrinsic contributions.

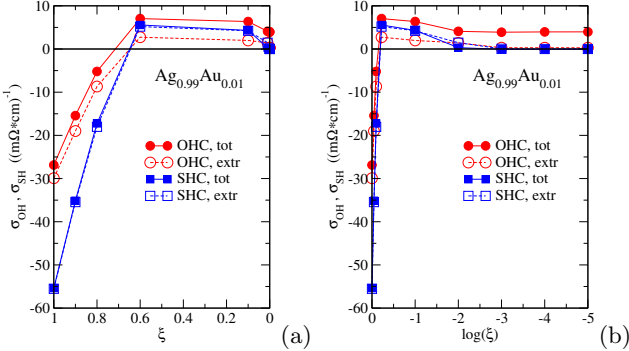


FIG. 7. The OHC and SHC $\text{Ag}_{0.99}\text{Au}_{0.01}$ as a function of the SOC scaling factor ξ . Figures (a) and (b) represent the same results plotted using linear and logarithmic meshes for ξ , respectively.

$\xi = 0$.

In the case of $\text{Rh}_{1-x}\text{Ag}_x$, the behavior of the OHE and SHE shown in Fig. 6 (b) (full symbols) is rather different when compared to $\text{Ag}_{1-x}\text{Au}_x$. First of all, the OHE and SHE at small impurity concentration are much smaller than in the case of $\text{Ag}_{1-x}\text{Au}_x$. Their extrinsic

contributions (open symbols) are negligibly small for an Ag concentration increasing above ≈ 0.5 at.%, where the OHE and SHE are mainly determined by the intrinsic contributions. Furthermore, the extrinsic OHE and SHE are negative and exhibit a slow increase in magnitude for $x \rightarrow 0$. This increase correlates with a slow increase of the electrical conductivity $\sigma_{\mu\mu}$ and therefore can be attributed to the skew-scattering effect. Plotting the total σ_{OH} and σ_{SH} versus $\sigma_{\mu\mu}$ in Fig. 6(d) (full symbols) and extrapolating the curves to the limit $\sigma_{\mu\mu} = 0$, one can easily see the leading role of the intrinsic contribution to the OHC and SHC in the superclean regime. Small values for the side-jump contributions can be deduced also from the extrapolation of the the extrinsic OHC and SHC (open symbols).

To gain insight into the origin of such a strong difference between the properties of the OHC and SHC of $\text{Ag}_{1-x}\text{Au}_x$ and $\text{Rh}_{1-x}\text{Ag}_x$, we have performed a set of calculations of the OH and SH conductivities for the materials having the same host but with different elements used for impurities. The calculations were done for $T = 0$ K. We consider three representative systems, $\text{Ir}_{0.999}M_{0.001}^{4d}$, $\text{Rh}_{0.999}M_{0.001}^{5d}$ and $\text{Nb}_{0.999}M_{0.001}^{5d}$, composed of the $4d$ impurities in $5d$ -metal host and the other way around, of $5d$ impurities in $4d$ -metal host. The corresponding OHC and SHC are plotted in Fig. 8. First of all, one can see for all doped materials, that the absolute values of the OHC are smaller than those of the SHE. The OHC obtained for $\text{Ir}_{0.999}M_{0.001}^{4d}$ and for $\text{Rh}_{0.999}M_{0.001}^{5d}$ have opposite sign. The same property is found also for the SHC. Such a behavior has been observed previously for SHC²⁰ and was attributed to the relative strength of the SOC associated with the host and impurity atoms. Some further features concerning the impact of the SOC on the OHC and SHC will be discussed also below.

Another prominent feature of the OHC and SHC shown in Figs. 8, is a strong enhancement of the OHC and the SHC in the case, when the impurity atoms have the number of valence electrons close to that of the host atoms. As one can see, it is a consequence of the enhancement of the extrinsic OHC and SHC representing the leading contributions to the total OHC and SHC.

To figure out the origin of such a behavior, we can consider the impact of different impurities on the electronic structure of the doped materials. For this purpose, Fig. 9 shows the Bloch spectral function (BSF) $A(\vec{k}, E)$ for selected $\text{Ir}_{0.99}M_{0.01}^{4d}$ compounds, plotted along the high-symmetry directions of the Brillouin zone (BZ). One can clearly see a smearing of the energy bands due to disorder, which is rather moderate in the case of $\text{Ir}_{0.99}\text{Rh}_{0.01}$, i.e., for the system with the host and impurity elements having the same number of valence electrons. The most prominent smearing is observed for $\text{Ir}_{0.99}\text{Mo}_{0.01}$ and $\text{Ir}_{0.99}\text{Ag}_{0.01}$ for which the OHC and SHC are the smallest among those shown in Fig. 8.

Thus, one can clearly see a correlation between the values of the OHC and SHC and the smearing of the electron energy bands (i.e. inverse lifetime) caused by dif-

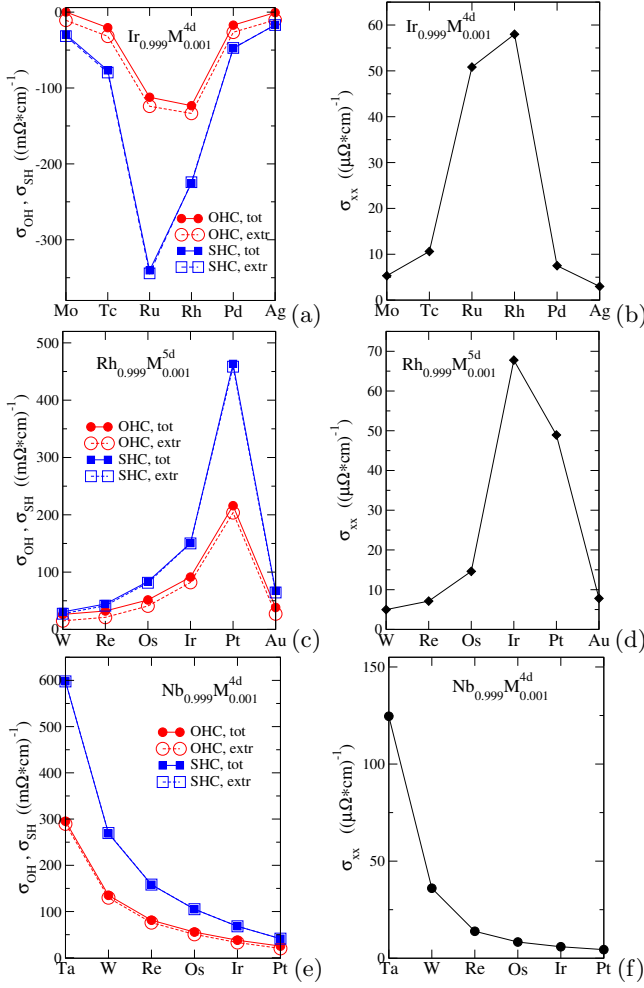


FIG. 8. (a), (c) and (e): OHC (circles) and SHC (squares) for $\text{Ir}_{0.999}M_{0.001}^{4d}$, $\text{Rh}_{0.999}M_{0.001}^{5d}$ and $\text{Nb}_{0.999}M_{0.001}^{4d}$, where total values are shown by full symbols, and extrinsic contributions - by open symbols. (b), (d) and (f) represent corresponding results for the longitudinal electrical conductivity $\sigma_{\nu\nu}$.

ferent types of impurities. We will discuss it in terms of the energy of the d -band scattering resonance E_d^M of the host and impurity atoms, varying across the transition metal period (see, e.g.⁴¹), which may be associated with the position of the center of d -band in metal. With this, the scattering strength V_s may be characterized by the distance between the centers of valence-electron d -bands of the host and impurity atoms, $V_s \sim \Delta_d$, that leads to estimate for the lifetime of the electron states $\tau \propto \Delta_d^{-2}$ (while $\tau^{-1} \propto \langle V_s^2 \rangle$ ¹⁴). This implies, that the weak smearing of the d -states, shown Fig. 9, should be small in the case of a small Δ_d , and should increase together with increasing Δ_d value, as it is inversely proportional to their lifetime τ . To visualize this trend for $\text{Ir}_{0.99}M_{0.01}$ materials, Fig. 10 shows the scattering phase shift $\delta_{l=2}(E)$ showing the d -resonances of the impurity and host atoms. Note that for simplicity reason the results are given for the non-relativistic case. The dashed line represents the

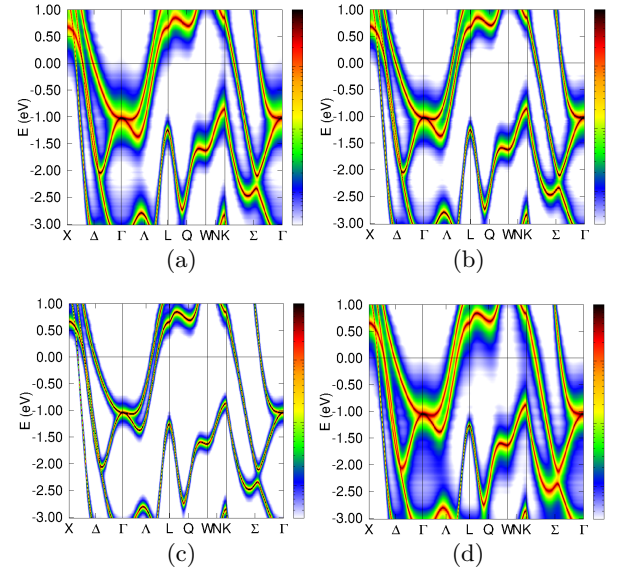


FIG. 9. BSF $A(E, \vec{k})$ for $\text{Ir}_{0.99}\text{Mo}_{0.01}$ (a) $\text{Ir}_{0.99}\text{Tc}_{0.01}$ (b) $\text{Ir}_{0.99}\text{Rh}_{0.01}$ (c) and $\text{Ir}_{0.99}\text{Ag}_{0.01}$ (d).

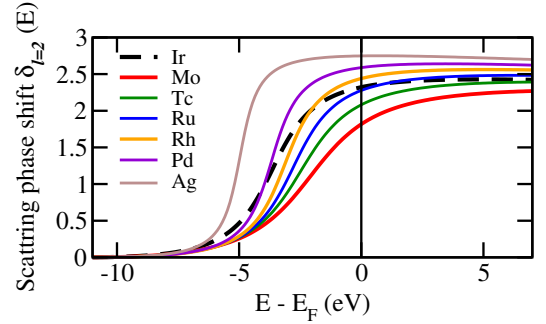


FIG. 10. Scattering phase shift $\delta_{l=2}(E)$ for $\text{Ir}_{0.99}M_{0.01}^{4d}$.

phase shift $\delta_{l=2}^{Ir}(E)$ for the host atom. As one can see, the position of the $4d$ -resonances of the impurity atoms changes when the impurity M is varied along the $4d$ period, crossing the resonance energy for the host Ir atom. The results shown in Fig. 10 are in line with the BSF plotted in Fig. 9. When the resonances are close to each other one can see the weakest scattering amplitude, e.g. in the case of $\text{Ir}_{0.99}\text{Rh}_{0.01}$ in contrast to $\text{Ir}_{0.99}\text{Ag}_{0.01}$ with $\Delta_d \approx 0.2$ eV and $\Delta_d \approx 1.6$ eV, respectively. Furthermore, using the estimate $\sigma_{\nu\nu} \propto \Delta_d^{-2}$ as discussed by Crépieux and Bruno¹⁴, one can get an idea on the impact of the type of impurity atom on the transport properties. Figs. 8(c) and (d) show the electrical conductivity for the $\text{Ir}_{0.999}M_{0.001}^{4d}$, $\text{Rh}_{0.999}M_{0.001}^{5d}$ and $\text{Nb}_{0.999}M_{0.001}^{4d}$ systems. In line with our discussions above, the maximum of the conductivity occurs in the case, when the distance Δ_d between the $4d$ and $5d$ resonances is minimal. On the other hand, the skew-scattering conductivity follows the relationship $\sigma_{\text{OH}/\text{SH}}^{\text{skew}} \propto \langle V_s \rangle^3 / \langle V_s^2 \rangle^2$ (see Ref. [14]). As

a consequence, this leads to $\sigma_{\text{OH/SH}}^{\text{skew}} \propto \Delta_d^{-1}$, i.e. to the element dependent enhancement of the OHC and SHC occurring in parallel with the enhancement of the electrical conductivity.

2. Temperature effect in doped systems

Next, we will discuss the impact of temperature induced lattice vibrations on the OHE and SHE for doped materials. Fig. 11 demonstrates the OHC (circles) and SHC (squares) for $\text{Ir}_{0.99}\text{Rh}_{0.01}$ (a) and $\text{Ir}_{0.99}\text{Au}_{0.01}$ (b), plotted as a function of temperature, and compared with the results for pure Ir. The most pronounced difference between the results for doped and undoped systems occurs at low temperature. This difference gradually vanishes in the high-temperature regime, when the OHC and SHC for doped and undoped systems approach the values mainly given by the intrinsic contributions. The strong temperature dependence of the OHC and SHC for $\text{Ir}_{0.99}\text{Rh}_{0.01}$ at low temperature (see Fig. 11 (a)) stems from the extrinsic skew-scattering contributions that quickly decrease at raising temperature. As $\sigma_{\text{OH/SH}}^{\text{skew}} \propto \langle V_s \rangle^3 / \langle V_s^2 \rangle^2$, at finite temperature the scattering potential can be split into 'atomic' and 'electron-phonon' parts. While the nominator $\langle V_s \rangle^3 \approx \langle V_a \rangle^3$, as $\langle V_{e-ph} \rangle = 0^{14}$, the denominator accounts for both types of scattering contributions, i.e. $\langle (V_a + V_{e-ph})^2 \rangle$, increasing with temperature due to an increasing amplitude of the lattice vibrations.

Thus, in the case of $\text{Ir}_{0.99}\text{Rh}_{0.01}$, a large value of the skew scattering conductivity at $T = 0$ K, $\sigma_{\text{OH/SH}}^{\text{skew}} \propto \frac{1}{x} \frac{1}{\Delta_d}^{14}$ with $\Delta_d \approx 0.2$ eV, decreases at finite temperature due to electron-phonon scattering (up to $\langle V_{e-ph}^2 \rangle^{1/2} \sim 0.1$ eV) according to $\sigma_{\text{OH/SH}}^{\text{skew}} \propto \langle V_a \rangle^3 / \langle (V_a + V_{e-ph}(T))^2 \rangle^2$. In the case of $\text{Ir}_{0.99}\text{Au}_{0.01}$, however (see Fig. 11(b)) $\Delta_d \gg V_{e-ph}$ as $\Delta_d \approx 1.6$ eV, leading to a weak dependence on temperature according to $\sigma_{\text{OH/SH}}^{\text{skew}} \propto \frac{1}{x} \frac{1}{\Delta_d} (1 - O(\langle V_{e-ph}^2 \rangle / \langle V_a^2 \rangle))$. At high temperature σ_{OH} and σ_{SH} approach the intrinsic OHC and SHC, as it was seen also for $\text{Ir}_{0.99}\text{Rh}_{0.01}$.

3. SOC effect

Finally, we demonstrate the impact on the OHC and SHC of only SOC-driven scattering events. For this, we consider a model system, $\text{Ir}_{0.999}\text{Ir}_{0.001}$, composed of the same type of atoms used for host as well as for impurity. In the case of unchanged SOC in the system, it is identical to pure Ir. However, using the parameter $\xi = c_0^2/c^2$ to scale speed of light at the impurity sites, one can create SOC-driven scattering potential given as follows

$$V_{\text{imp}}^{\text{SOC}} = (\xi - 1) \frac{1}{2m^2 c_0^2 r} \frac{\partial V}{\partial r} (\hat{s} \cdot \hat{l}), \quad (6)$$

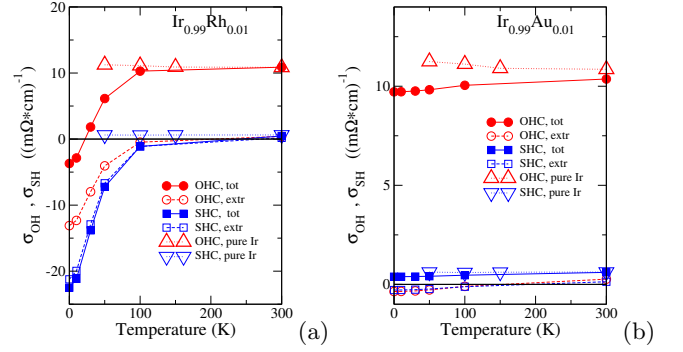


FIG. 11. OH (circles) and SH (squares) conductivities for $\text{Ir}_{0.99}\text{Rh}_{0.01}$ (a) and $\text{Ir}_{0.99}\text{Au}_{0.01}$ (b) plotted as a function of temperature. Full symbols represent total values calculated accounting for vertex corrections, while open symbols show only the extrinsic contribution to the OHC and SHC. Triangles represent the results on the OHC and SHC for pure Ir.

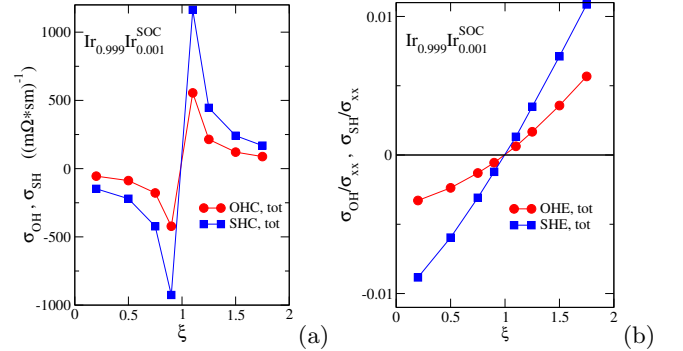


FIG. 12. The OH and SH conductivities for $\text{Ir}_{0.999}\text{Ir}_{0.001}^{\text{SOC}}$, i.e. for Ir impurities in Ir with the speed of light scaled by a factor ξ^{-1} : (a) absolute values of OHC and SHC and (b) OHC and SHC are divided by electrical conductivity, i.e. $\sigma_{\text{OH}}/\sigma_{xx}$ and $\sigma_{\text{SH}}/\sigma_{xx}$.

with $\hat{s} = \frac{\hbar}{2} \vec{\sigma}$ and \hat{l} being the operators of spin and orbital angular momentum. Fig. 12 (a) represent the results on the OHC and SHC for such a system, plotted as a function of scaling factor ξ . One can see a divergence of both the OH and SH conductivities, σ_{OH} and σ_{SH} in the limit of $\xi - 1 \rightarrow \pm 0$, with opposite signs for $\xi < 1$ and $\xi > 1$, arising due to extrinsic contributions. This behavior is a consequence of vanishing scattering potential in the case of $\xi = 1$ leading also to a divergence of the electrical conductivity. Assuming that the behavior of both extrinsic OH and SH conductivities are determined by skew scattering and are proportional to electrical resistivity, the ratios $\sigma_{\text{OH}}/\sigma_{xx}$ and $\sigma_{\text{SH}}/\sigma_{xx}$ should be smooth functions of scaling factor ξ , that can be seen in Fig. 12 (b). These results also ensure a common origin of the extrinsic OH and SH conductivities. Also, these results demonstrate a dependence of the sign of these quantities on the relative values of SOC corresponding to the host atoms and to impurities.

IV. SUMMARY

To summarize, the OHC calculated for non-magnetic 3*d*-, 4*d*- and 5*d*-metals, elemental and doped, is compared with corresponding results on the SHC. A strong difference has been found for the temperature dependence of the OHC and SHC for undoped and doped systems. For elemental systems at finite temperature, the electron-phonon skew scattering has a negligible impact on the extrinsic OHC and SHC. As a consequence, the OHC and SHC and their temperature dependent variation is determined mainly by the intrinsic contributions. Moreover, different temperature dependent behavior of the intrinsic SOC-independent OHC and SOC-driven SHC indicates non-trivial relationship between these quantities. In doped materials, the extrinsic contribution to the OHC and SHC is dominating at low temperature.

However, a strong decrease is found for higher temperatures due to the increasing impact of the electron-phonon scattering.

ACKNOWLEDGMENTS

The authors thank Erna Delczeg for bringing our attention to the subject studied in the work, as well as for useful discussions.

Appendix A: Kubo-Bastin equation

The so-called Bastin formula for the response quantity σ is given by the following equation²⁴

$$\sigma_{\mu\nu} = \frac{i\hbar}{V} \int_{-\infty}^{\infty} dE f(E) \text{Tr} \left\langle \hat{J}_{\mu} \frac{dG^{+}(E)}{dE} \hat{j}_{\nu} \delta(E - \hat{H}) - \hat{J}_{\mu} \delta(E - \hat{H}) \hat{j}_{\nu} \frac{dG^{-}(E)}{dE} \right\rangle_c \quad (\text{A1})$$

with $\nu = (x, y, z)$ denoting Cartesian coordinates, $f(E)$ the Fermi-Dirac distribution function and $G^{\pm}(E) = (E - \hat{H} \pm i\delta)^{-1}$ the retarded and advanced Green's function operators. The equation describes the response of an observable represented by an operator \hat{J}_{μ} to the perturbation represented by the operator \hat{j}_{ν} . The brackets $\langle \dots \rangle$ denotes a configurational average in the presence of any type of disorder. For the case $T = 0$ K, this expression can be transformed to the following form⁴²:

$$\begin{aligned} \sigma_{\mu\nu}^{\xi} &= \frac{\hbar}{4\pi\Omega} \left[\text{Trace} \left\langle \hat{J}_{\mu}^{\xi} (\hat{G}^{+} - \hat{G}^{-}) \hat{j}_{\nu} \hat{G}^{-} - \hat{J}_{\mu}^{\xi} \hat{G}^{+} \hat{j}_{\nu} (\hat{G}^{+} - \hat{G}^{-}) \right\rangle \right. \\ &\quad \left. + \int_{-\infty}^{E_F} d\varepsilon \text{Trace} \left\langle \hat{J}_{\mu}^{\xi} \hat{G}^{+} \hat{j}_{\nu} \frac{d\hat{G}^{+}}{d\varepsilon} - \hat{J}_{\mu}^{\xi} \frac{d\hat{G}^{+}}{d\varepsilon} \hat{j}_{\nu} \hat{G}^{+} - \left(\hat{J}_{\mu}^{\xi} \hat{G}^{-} \hat{j}_{\nu} \frac{d\hat{G}^{-}}{d\varepsilon} - \hat{J}_{\mu}^{\xi} \frac{d\hat{G}^{-}}{d\varepsilon} \hat{j}_{\nu} \hat{G}^{-} \right) \right\rangle \right] = \sigma_{\mu\nu}^{I\xi} + \sigma_{\mu\nu}^{II\xi} \quad (\text{A2}) \end{aligned}$$

The first term is evaluated at the Fermi energy E_F and contains contributions only from the Fermi surface and is referred to as Fermi-surface term. The second term implies an integration over all occupied states and is called Fermi-sea term. Within the multiple-scattering or KKR formalism, the real-space Green's function $G(\vec{r}, \vec{r}', E)$ is given by the expression²⁵:

$$\begin{aligned} G(\vec{r}, \vec{r}', E) &= \sum_{\Lambda_1 \Lambda_2} Z_{\Lambda_1}^n(\vec{r}, E) \tau_{\Lambda_1 \Lambda_2}^{nn'}(E) Z_{\Lambda_2}^{n' \times}(\vec{r}', E) \\ &\quad - \sum_{\Lambda_1} \left[Z_{\Lambda_1}^n(\vec{r}, E) J_{\Lambda_1}^{n \times}(\vec{r}', E) \Theta(r' - r) \right. \\ &\quad \left. J_{\Lambda_1}^n(\vec{r}, E) Z_{\Lambda_1}^{n \times}(\vec{r}', E) \Theta(r - r') \right] \delta_{nn'}. \quad (\text{A4}) \end{aligned}$$

Here \vec{r}, \vec{r}' refer to site n and n' , respectively, $\tau_{\Lambda \Lambda'}^{nn'}(E)$ is the so-called scattering path operator that transfers an

electronic wave coming in at site n' into a wave going out from site n with all possible intermediate scattering events accounted for. The four-component wave functions $Z_{\Lambda}^n(\vec{r}, E)$ ($J_{\Lambda}^n(\vec{r}, E)$) are regular (irregular) solutions to the single-site Dirac equation⁴³ with the Hamiltonian set up within the framework of relativistic spin-density functional theory^{44,45}:

$$\mathcal{H}_D = -ic\vec{\alpha} \cdot \vec{\nabla} + \frac{1}{2} c^2(\beta - 1) + V(\vec{r}) + \beta\vec{\sigma} \cdot \vec{B}_{xc}(\vec{r}). \quad (\text{A5})$$

These functions are labeled by the combined quantum numbers Λ ($\Lambda = (\kappa, \mu)$), with κ and μ being the spin-orbit and magnetic quantum numbers⁴⁶. The superscript \times indicates the left hand side solution of the Dirac equation. The operators α_i and β in the Hamiltonian in Eq. (A5) are the standard Dirac matrices⁴⁶ while $\vec{V}(\vec{r})$ and $\vec{B}_{xc}(\vec{r})$ are the spin independent and dependent parts of

the electronic potential^{25,46}.

In the case of disordered systems, the configurational average in the expression for the response tensor in Eq. [A2], $\langle JG^\pm jG^\pm \rangle \approx \langle JG^\pm \rangle \langle jG^\pm \rangle$, is performed making use of a configurational average of the single-particle Green function in the spirit of the coherent potential approximation (CPA) alloy theory, and accounting for the vertex corrections referring to two-particle quantities in the expression for the conductivity. Formally a corresponding response tensor element may be written as follows²⁰ (omitting the angular momentum indices):

$$\sigma_{\mu\nu}^{\text{VC}} \propto \text{Tr} J_\mu(z_2, z_1) (1 - \chi w)^{-1} \chi j_\nu(z_1, z_2). \quad (\text{A6})$$

$$\sigma_{\mu\nu}^{\text{NVC}} \propto \text{Tr} J_\mu(z_2, z_1) \chi j_\nu(z_2, z_1) \quad (\text{A7})$$

with the term $(1 - \chi w)^{-1}$ accounting for vertex corrections²⁷. Accordingly, VC and NVC denotes the response quantity including and excluding, respectively, the vertex corrections. The auxiliary quantity χ in Eqs.

(A6) and (A7) is given by

$$\begin{aligned} & \chi_{\Lambda_1 \Lambda_2 \Lambda_3 \Lambda_4}(z_1, z_2) \\ &= \frac{1}{\Omega_{\text{BZ}}} \int_{\text{BZ}} d^3k \tau_{\text{CPA}, \Lambda_1 \Lambda_2}(\mathbf{k}, z_1) \tau_{\text{CPA}, \Lambda_3 \Lambda_4}(\mathbf{k}, z_2) \\ & \quad - \tau_{\text{CPA}, \Lambda_1 \Lambda_2}^{\text{00}}(z_1) \tau_{\text{CPA}, \Lambda_3 \Lambda_4}^{\text{00}}(z_2), \end{aligned} \quad (\text{A8})$$

and the interaction term w is defined as

$$w_{\Lambda_1 \Lambda_2 \Lambda_3 \Lambda_4}(z_1, z_2) = \sum_{\alpha} x_{\alpha} x_{\Lambda_1 \Lambda_2}^{\alpha}(z_1) x_{\Lambda_3 \Lambda_4}^{\alpha}(z_2) \quad (\text{A9})$$

with

$$\underline{x}^{\alpha}(z) = \left\{ [\underline{t}_{\alpha}^{-1}(z) - \underline{t}_{\text{CPA}}^{-1}(z)]^{-1} + \underline{\tau}_{\text{CPA}}^{\text{00}}(z) \right\}, \quad (\text{A10})$$

where \underline{t}_{α} and $\underline{t}_{\text{CPA}}$ represent the single site t -matrix for atom type α and for the CPA medium, respectively, and $\underline{\tau}_{\text{CPA}}$ denotes the CPA averaged τ matrix. More details can be found in Ref. [42].

Following Butler's scheme²⁷, a response tensor may be spitted into a site-diagonal term $\sigma_{\mu\nu}^0 \propto \langle J^{0\mu} \tau^{00} j^{0\nu} \tau^{00} \rangle$ and site-off-diagonal term $\sigma_{\mu\nu}^1 \propto \langle J^{n\mu} \tau^{nm} j^{m\nu} \tau^{mn} \rangle$ ^{20,27}, such that the former term is purely coherent. Furthermore, according to the findings by Turek et al.³⁷ concerning the SHC, the vertex corrections to the site-off-diagonal Fermi sea term is negligible. This implies at the end, that the extrinsic SHC is dominated by the Fermi surface contribution, $\sigma_{\mu\nu}^1(E_F)$.

-
- ¹ J. Sinova, S. O. Valenzuela, J. Wunderlich, C. H. Back, and T. Jungwirth, *Rev. Mod. Phys.* **87**, 1213 (2015).
- ² B. A. Bernevig, T. L. Hughes, and S.-C. Zhang, *Phys. Rev. Lett.* **95**, 066601 (2005).
- ³ H. Kontani, T. Tanaka, D. S. Hirashima, K. Yamada, and J. Inoue, *Phys. Rev. Lett.* **102**, 016601 (2009).
- ⁴ D. Go, H.-W. Lee, P. M. Oppeneer, S. Blügel, and Y. Mokrousov, *Phys. Rev. B* **109**, 174435 (2024).
- ⁵ T. Tanaka, H. Kontani, M. Naito, T. Naito, D. S. Hirashima, K. Yamada, and J. Inoue, *Phys. Rev. B* **77**, 165117 (2008).
- ⁶ S. Han, H.-W. Lee, and K.-W. Kim, *Current Applied Physics* **50**, 13 (2023).
- ⁷ D. Go, D. Jo, C. Kim, and H.-W. Lee, *Phys. Rev. Lett.* **121**, 086602 (2018).
- ⁸ J. Sinova, D. Culcer, Q. Niu, N. A. Sinitsyn, T. Jungwirth, and A. H. MacDonald, *Phys. Rev. Lett.* **92**, 126603 (2004).
- ⁹ H. Kontani, T. Tanaka, D. S. Hirashima, K. Yamada, and J. Inoue, *Phys. Rev. Lett.* **100**, 096601 (2008).
- ¹⁰ L. Salemi, M. Berritta, A. K. Nandy, and P. M. Oppeneer, *Nature Communications* **10**, 5381 (2019).
- ¹¹ D. Go, D. Jo, H.-W. Lee, M. KlÄÄrui, and Y. Mokrousov, *Europhysics Letters* **135**, 37001 (2021).
- ¹² Y.-G. Choi, D. Jo, K.-H. Ko, D. Go, K.-H. Kim, H. G. Park, C. Kim, B.-C. Min, G.-M. Choi, and H.-W. Lee, *Nature* **619**, 52 (2023).
- ¹³ I. Lyalin, S. Alikhah, M. Berritta, P. M. Oppeneer, and R. K. Kawakami, *Phys. Rev. Lett.* **131**, 156702 (2023).
- ¹⁴ A. Crépieux and P. Bruno, *Phys. Rev. B* **64**, 094434 (2001).
- ¹⁵ J. Inoue, G. E. W. Bauer, and L. W. Molenkamp, *Phys. Rev. B* **70**, 041303 (2004).
- ¹⁶ P. Tang and G. E. W. Bauer, "Role of disorder in the intrinsic orbital hall effect," (2024), arXiv:2401.17620 [cond-mat.mes-hall].
- ¹⁷ H. Liu and D. Culcer, *Phys. Rev. Lett.* **132**, 186302 (2024).
- ¹⁸ A. Hoffmann, *IEEE Trans. Magn.* **49**, 5172 (2013).
- ¹⁹ F. Zheng, M. Zhu, J. Dong, X. Li, Y. Zhou, K. Wu, and J. Zhang, *Phys. Rev. B* **109**, 224401 (2024).
- ²⁰ S. Lowitzer, *Relativistic electronic transport theory - The spin Hall effect and related phenomena*, Ph.D. thesis, LMU München (2010).
- ²¹ S. Lowitzer, D. Ködderitzsch, and H. Ebert, *Phys. Rev. B* **82**, 140402(R) (2010).
- ²² S. Lowitzer, M. Gradhand, D. Ködderitzsch, D. V. Fedorov, I. Mertig, and H. Ebert, arXiv:1010.5520v1 (2010).
- ²³ S. Lowitzer, M. Gradhand, D. Ködderitzsch, D. V. Fedorov, I. Mertig, and H. Ebert, *Phys. Rev. Lett.* **106**, 056601 (2011).
- ²⁴ A. Bastin, C. Lewiner, O. Betbeder-matibet, and P. Nozieres, *Journal of Physics and Chemistry of Solids* **32**, 1811 (1971).
- ²⁵ H. Ebert, J. Braun, D. Ködderitzsch, and S. Mankovsky, *Phys. Rev. B* **93**, 075145 (2016).
- ²⁶ H. Ebert et al., *The Munich SPR-KKR package*, version 8.5, <https://www.ebert.cup.uni-muenchen.de/en/software-en/13-sprkk> (2020).

- ²⁷ W. H. Butler, Phys. Rev. B **31**, 3260 (1985).
- ²⁸ S. Onoda, N. Sugimoto, and N. Nagaosa, Phys. Rev. B **77**, 165103 (2008).
- ²⁹ S. Onoda, N. Sugimoto, and N. Nagaosa, Phys. Rev. Lett. **97**, 126602 (2006).
- ³⁰ N. A. Sinitsyn, J. Phys.: Cond. Mat. **20**, 023201 (2008).
- ³¹ K. Chadova, S. Wimmer, H. Ebert, and D. Ködderitzsch, Phys. Rev. B **92**, 235142 (2015).
- ³² J. Banhart, A. Vernes, and H. Ebert, Solid State Commun. **98**, 129 (1996).
- ³³ H. Ebert, D. Ködderitzsch, and J. Minár, Rep. Prog. Phys. **74**, 096501 (2011).
- ³⁴ S. H. Vosko, L. Wilk, and M. Nusair, Can. J. Phys. **58**, 1200 (1980), <http://www.nrcresearchpress.com/doi/pdf/10.1139/p80-159>.
- ³⁵ H. Ebert, S. Mankovsky, K. Chadova, S. Polesya, J. Minár, and D. Ködderitzsch, Phys. Rev. B **91**, 165132 (2015).
- ³⁶ L. Salemi and P. M. Oppeneer, Phys. Rev. Mater. **6**, 095001 (2022).
- ³⁷ I. Turek, J. Kudrnovský, and V. Drchal, Phys. Rev. B **100**, 134435 (2019).
- ³⁸ L. Berger and G. Bergmann, “THE HALL EFFECT OF FERROMAGNETS,” in *The Hall Effect and Its Applications*, edited by C. L. Chien and C. R. Westgate (Springer Science+Business Media, LLC, 1980) pp. 55–76.
- ³⁹ M. Isasa, E. Villamor, L. E. Hueso, M. Gradhand, and F. Casanova, Phys. Rev. B **91**, 024402 (2015), erratum: Phys. Rev. B **92**, 019905 (2015).
- ⁴⁰ G. V. Karnad, C. Gorini, K. Lee, T. Schulz, R. Lo Conte, A. W. J. Wells, D.-S. Han, K. Shahbazi, J.-S. Kim, T. A. Moore, H. J. M. Swagten, U. Eckern, R. Raimondi, and M. Kläui, Phys. Rev. B **97**, 100405 (2018).
- ⁴¹ G. M. Stocks, R. W. Williams, and J. S. Faulkner, Phys. Rev. Lett. **26**, 253 (1971).
- ⁴² D. Ködderitzsch, K. Chadova, and H. Ebert, Phys. Rev. B **92**, 184415 (2015).
- ⁴³ E. Tamura, Phys. Rev. B **45**, 3271 (1992).
- ⁴⁴ A. H. MacDonald and S. H. Vosko, J. Phys. C: Solid State Phys. **12**, 2977 (1979).
- ⁴⁵ E. Engel and R. M. Dreizler, *Density Functional Theory – An advanced course* (Springer, Berlin, 2011).
- ⁴⁶ M. E. Rose, *Relativistic Electron Theory* (Wiley, New York, 1961).